This manuscript was accepted by J. Appl. Phys. Click here to see the version of record.

High Pressure High Temperature Devitrification of $Fe_{78}B_{13}Si_9$ Metallic Glass with Simultaneous X-ray Structural Characterization

Andrew K. Stemhorn,[1] Yogesh K. Vohra,[1] and Spencer J. Smith[1]

Department of Physics, University of Alabama at Birmingham, Birmingham, AL 35294, USA

Changes in bulk crystallization behavior following devitrification at high pressure are investigated for a $Fe_{78}B_{13}Si_9$ composition metallic glass using *in-situ* energy dispersive x-ray powder diffraction. Crystallization with time was evaluated for a series of measurements to a maximum pressure of 5.63 ± 0.15 GPa for the $Fe_{78}B_{13}Si_9$ glass. Pressure was found to strongly affect onset bulk crystallization temperature T_x. Crystallization at each pressure was found to progress in two stages. In the first stage α-Fe precipitates and in the second Fe_2B forms while α-Fe continues to crystallize. Complementary high pressure room temperature studies were conducted.

Keywords: x-ray diffraction, metallic glasses, crystallization, phase transformation kinetics, high pressure

This manuscript was accepted by J. Appl. Phys. Click here to see the version of record.

I. INTRODUCTION

Metallic glasses demonstrate superior material properties and show great potential for science and industrial applications[1,2], but require considerable cooling rates to form. Alloys demonstrating a diminished critical cooling rate are often comprised of uncommon or expensive elemental compositions, such as those composed of palladium or rare earth elements as principal constituents or are intrinsically brittle showing inadequate plasticity and demonstrating poor fracture strength limiting potential viable application[3] or lack work hardening ability further limiting potential longevity of metallic glass components[4]. Some of these weakness can be improved by developing composites made by introducing intrinsic particulate to the melt prior to casting, crystallized from the source material during casting or by devitrifying and partially crystallizing the material[3,5]. The present study explores the role of pressure in the devitrification and crystallization of a monolithic metallic glass and may be useful in creating nano-composites where pressure is utilized as an additional control parameter in heating a partial crystallizing the glass[6,7].

Packing density of an amorphous phase is generally linked to glass forming ability[8–10], but correlation between density and glass forming ability has not been extensively demonstrated experimentally[11,12]. Understanding kinetics of bulk crystallization of metallic glasses is of principal importance in understanding metallic glass formation[1,13,14], overcoming weaknesses and important for the formation of precipitant type nano-composites[15]. High pressure studies of metallic glasses may offer insight in to the role of density in glass transition behavior and glass forming ability. Additionally, glass behavior during devitrification near or around the glass transition involves sluggish bulk crystallization kinetics permitting a detailed study of material properties and bulk crystallization behavior on a laboratory time scale[16,17]. Finally, high pressure die casting may be an important tool for the manufacture of metallic glass components[18,19]. The described work illustrates properties of metallic glasses which could limit the applicability of high pressure die casting when used on similar alloys.

Ambient pressure devitrification and bulk crystallization kinetics studies of various Fe-Si-B composition metallic glasses summarized by Illeková et al.[20] demonstrate Fe-Si-B metallic glass system generally exhibit a two stage bulk crystallization following devitrification and higher onset bulk crystallization temperature T_x is observed with higher percentage boron and a smaller temperature separation of the two stages. The effect of increased pressure on bulk crystallization kinetics of glasses in general demonstrate an over all trend of in-

crease in bulk onset crystallization temperature following devitrification with the exception of a few notable examples of materials that exhibit negative pressure dependence of T_x for some range of pressure such as amorphous selenium or albite. Various compositions of metallic glass have displayed a dip or a short lived negative pressure dependence ($dT_x/dP < 0$) followed by a subsequent rise and return to positive pressure dependence ($dT_x/dP < 0$) of the onset bulk crystallization temperature T_x as dependent on rise in pressure including $Zr_{41}Ti_{14}Cu_{12.5}Ni_{10}Be_{22.5}$[21] with the dip centered between 5.6 GPa and 6.5 GPa, $Al_{89}La_6Ni_5$[22] with the minimum around one GPa and $Fe_{72}P_{11}C_6Al_5B_4Ga_2$ over the range 2.4 to 3.9 GPa. The two stage bulk crystallization was confirmed for the same $Fe_{78}B_{13}Si_9$ composition examined in this study at ambient pressure separately by Tong et al.[7] and Bang et al.[23]. The present study examines the effects of pressure on bulk onset crystallization temperature for a $Fe_{78}B_{13}Si_9$ metallic glass composition at high pressure and high temperature.

II. EXPERIMENT

The iron boron silicon composition metallic glass $Fe_{78}B_{13}Si_9$ purchased through Goodfellows was examined as representative of this class of metallic glasses. After devitrification and bulk crystallization, simple ternary alloys have a distinct advantage of having fewer end product phases diminishing ambiguity in crystallographic analysis. Additionally, the $Fe_{78}B_{13}Si_9$ composition of metallic glass is extensively studied and characterized at ambient pressure making $Fe_{78}B_{13}Si_9$ a logical choice for study at high pressure.

A. High Pressure Ambient Temperature

The sample was evaluated at high pressure and ambient temperature using *in-situ* angular dispersive x-ray diffraction and an image-plate area detector. The experiments were conducted at the Advanced Photon Source (APS) high pressure collaborative access team (HPcat) sector 16, Argonne National Laboratory (ANL) in Chicago[24]. Fit2D was used in integration of the image plate data and to correct for polarization and geometric factors[25]. High pressure x-ray structural measurements for $Fe_{78}B_{13}Si_9$ were carried out at HPcat BM-D using a 0.424603 Å wavelength incident beam with a sample to detector distance was 318 mm. The incident beam cross-section was 24 μm vertical and 11 μm horizontal full width at

This manuscript was accepted by J. Appl. Phys. Click here to see the version of record.

half maximum. For the experiment two opposing 300 μm diameter cutlets were used with a pre-indented spring steel gasket and a 80 μm cylindrical sample cavity. Copper foil was placed within the sample chamber as a pressure marker. Pressure was evaluated using the Birch-Murnaghan equation of state[26] of copper with the zero pressure ambient temperature unit cell constant a = 3.6148 Å, bulk modulus $B_o = 121.6\ GPa$ and the first derivative B' = 5.583[27]. A series of spectra are taken to a maximum pressure of 65.0 GPa. An additional series of measurements were taken without a pressure marker. Pressure was determined by comparison of first amorphous peak position to the pressure marker series. For $Fe_{78}B_{13}Si_9$ no compression induced bulk crystallization was apparent in the amorphous profile to the maximum pressure.

B. High Pressure High Temperature

High pressure high temperature structural measurements were performed at ANL APS HPcat beam line 16BM-B synchrotron radiation source[28]. Pressure was generated using a Paris Edinburgh type large volume press with tungsten carbide conical anvils. The setup includes a custom made heater gasket assembly described here[29]. For each run ten $1 \times 1\, mm$ sections of metallic glass foil were stacked in the boron nitrate (BN) crucible. The BN cylinder was surrounded by the cylindrical graphite resistive heater. The cell gasket assembly contains a magnesium oxide (MgO) internal pressure standard. Temperature was elevated by increasing power supplied to the gasket heater. Structure was evaluated using an *in-situ* $100 \times 100\, \mu m$ cross sectional area parallel white incident x-ray excitation beam with a 1-120 keV 4000 channel germamium x-ray radiation detector. The detector was set 15 degrees from the incident beam path. Power, voltage and current are recorded with time and stored in an experiment meta file. Energy dispersive x-ray diffraction spectra were recorded at 20 second intervals and stored as independent files.

The methodology of the experiment was chosen to reflect constant heating rate differential scanning calorimetry[30]. The setup was taken to elevated pressure prior to heating. Each run was initially heated to 300℃ as a common starting temperature. From 300℃ power was increased incrementally at a rate of one Watt every 80 seconds to the maximum temperature for each run. To measure pressure, a series of MgO spectra are taken before the T_x bulk crystallization begins and then immediately after the bulk crystallization was complete and the x-ray spectra show no the apparent further change. To measure MgO, the cell was

moved with respect to the incident beam path until only the MgO x-ray profile was visible. After measuring the trailing MgO spectra, the Paris Edinburgh cell was cooled to ambient temperature and de-pressurized. A final spectrum of the devitrified fully crystallized sample at ambient pressure and temperature was collected for structural evaluation. The final spectra was exposed for a 10 minute or greater collection time. A single implementation of the described method is executed for each pressure.

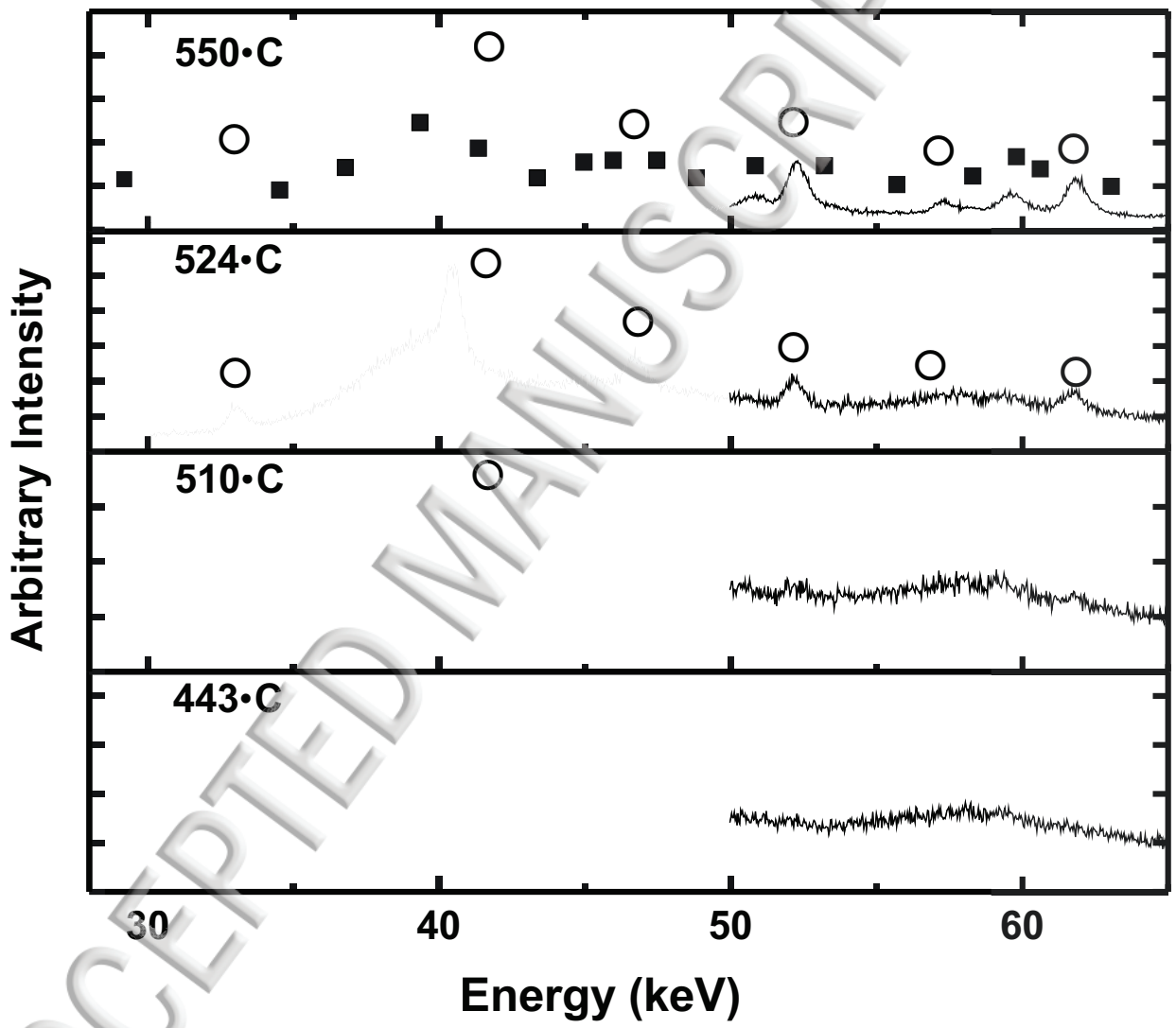

FIG. 1. Distinct phases of $Fe_{78}B_{13}Si_9$ at 0.57 ± 0.21 GPa during devitrification are shown. The temperature displayed is the middle of five averaged spectra. α-Fe peaks are indexed with circles. For 550℃ the tetragonal Fe_2B peaks are indicated with solid squares.

Temperature was calculated using the cell pressure, power, voltage and current; for each time in the experiment meta file[28,29]. The recorded time for each 20 second x-ray spectra was used to determine temperature by interpolation from the meta file temperatures. An

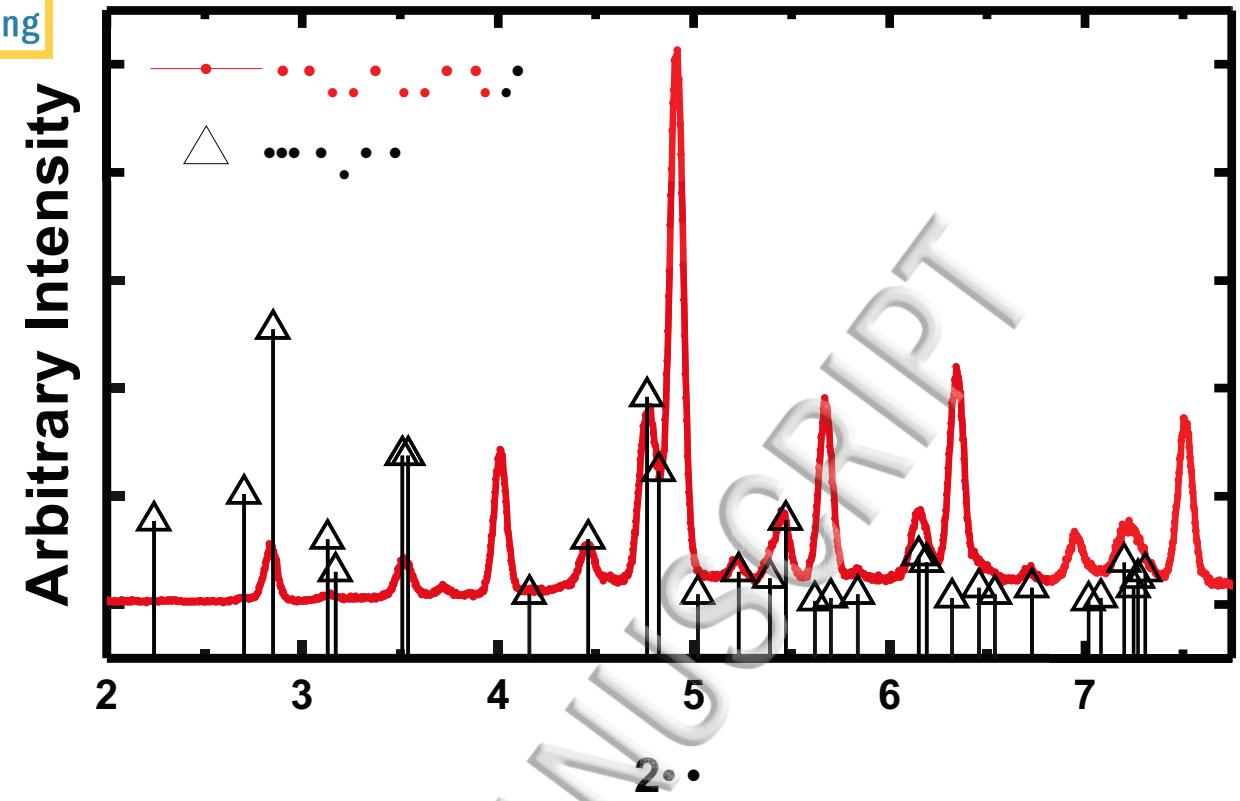

FIG. 2. Graph displays $Fe_{78}B_{13}Si_9$ after devitrification at 0.57 ± 0.21 *GPa*. The listed JCPDS 361332 tetragonal Fe_2B peaks are overlaid.

example of the datasets is shown in figure 3 with the interpolated temperature for each point. Pressure was determined using the Mie-Gruneisen-Einstein approach for MgO as derived by Kono et al.[31] and for comparison using a version prepared by Dorogokupets et al.[32]. The two scales are compared by Ye et al.[33]. The x-axis for each spectra was converted from keV to 2θ with a virtual wavelength of 0.1 Å for analysis[34]. The unit cell volume for each MgO spectra was evaluated using the program CMPR[35] and PowderCell[36]. Pressure was assumed linear with respect to time from the range between the MgO measurements preceding and following the bulk crystallization of the sample. The MgO spectra preceding T_x were taken near 500℃ for the two highest pressure $Fe_{78}B_{13}Si_9$ spectra. The other MgO spectra preceding T_x in each run were taken at 450℃. The trailing MgO spectra was taken after complete bulk crystallization and the x-ray spectra showed no the apparent further change. In all runs the pressure change was less 0.1 *GPa* in the time between onset bulk crystallization to completion.

This manuscript was accepted by J. Appl. Phys. Click here to see the version of record.

III. RESULTS

Each phase observed through devitrification persists to ambient conditions. As observed with ambient pressure devitrification studies bulk crystallization for each pressure occurs in two stages. The first stable phase to precipitate in every run is identified as α-Fe or BCC iron shown in figure 1. The α-Fe phase is observed as the first stable phase to precipitate under various conditions for Fe-based metallic glasses[17,20,23,37–41]. For Si containing alloys, the α-Fe phase is often cited as α-(Fe,Si) to indicate disordered incorporation of silicon into the BCC iron phase[7,20,42,43]. The α-Fe phase was indexed with JCPDS database number 060696, Space group (229) $Im\bar{3}m$, with a lattice parameter a = 2.8664 Å[44]. The second stage of bulk crystallization was identified as primarily tetragonal Fe_2B. The tetragonal Fe_2B second phase was observed to precipitate for Fe-based metallic glasses under various conditions[20,23,37,39–41,43]. For the binary Fe_xB system, Wang et al. observed that the most stable end products are Fe_2B and α-Fe[39]. The tetragonal Fe_2B phase was indexed as JCPDS database number 361332, Space group I4/mcm (140), with lattice parameters a = 5.1103 Å and b = 4.2494 Å. Depending on pressure a minor phase appears in the second stage during bulk crystallization. The second stage of bulk crystallization consists entirely of tetragonal Fe_2B for $Fe_{78}B_{13}Si_9$ devitrified at pressures 0.57 ± 0.21 GPa, 1.77 ± 0.12 GPa and 5.63 ± 0.15 GPa. A mixed second stage consisting of primarily tetragonal Fe_2B and a minority phase was found in $Fe_{78}B_{13}Si_9$ for devitrification pressures 0.65 ± 0.20 GPa, 2.76 ± 20 GPa and 4.59 ± 0.09 GPa.

Figure 2 shows the 0.57 ± 0.21 GPa devitrification of the $Fe_{78}B_{13}Si_9$ sample after the run is complete. The peak intensities of the minority second phase are insufficient for classification. Figure 1 illustrates the various stages of bulk crystallization. Each EDXD pattern consists of five 20 second spectra added together to increase resolution and decrease white noise. The temperature displayed is in the middle of five averaged spectra. At 443℃ the glass was well below the observed bulk crystallization temperature of 510℃ and was still amorphous. The 510℃ pattern shows the α-Fe phase starting to grow from the amorphous background. By 524℃ the α-Fe phase was distinctly visible while the amorphous pattern has diminished. At 550℃ the second stage tetragonal Fe_2B phase was visible and the amorphous profile is no longer present in the pattern.

In each run the α-Fe phase x-ray peaks continue to increase in intensity while the second phase x-ray peaks appear and the gain intensity. The intensity of the 200 α-Fe crystalline

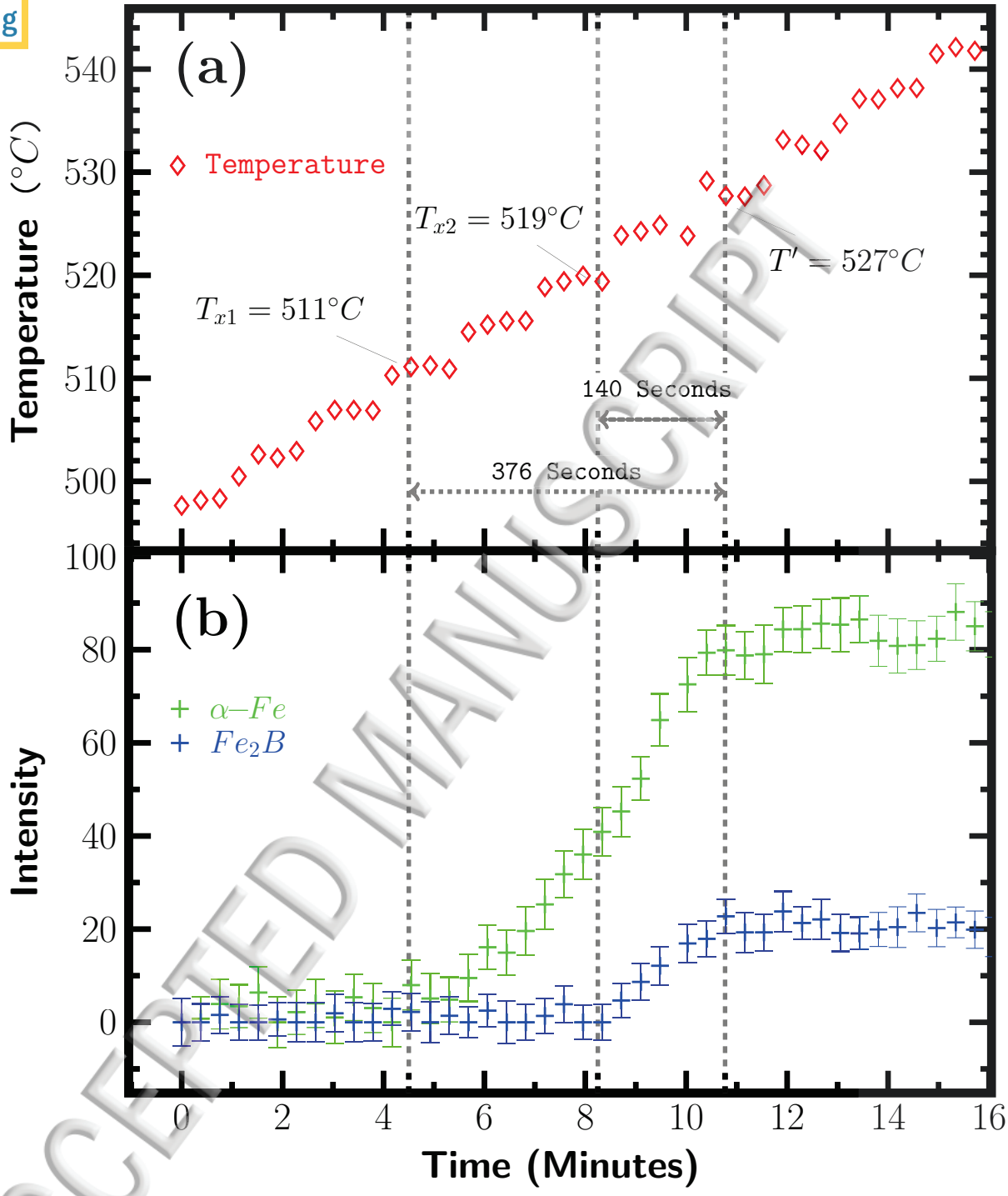

FIG. 3. pressure 0.57 ± 0.21 *GPa* $Fe_{78}B_{13}Si_9$, (a) Temperature for the 20 second spectra. (b) The peak intensity for the two phases during bulk crystallization. T_{x1} is the onset temperature for the α-Fe phase. T_{x2} is the onset temperature for the tetragonal Fe_2B. T' is the termination point for the transformation. Error for temperature and time are within the markers for each graph.

peak was fitted to reflect bulk crystallization following devitrification in the first and second

stage of bulk crystallization. The combined 202/310 peak for the tetragonal Fe_2B phase was fit to reflect progress of progress of bulk crystallization of Fe_2B in the second stage of bulk crystallization. Both peaks are distinct separate from all other observed peaks throughout the devitrification Figure 3 shows an example of a single bulk crystallization profile of each sample at lowest pressure an is a representative correlation of temperature, time and bulk crystallization at one pressure for each sample. The error bars represent the standard error for the Gaussian function fit after polynomial background subtraction. For each run, after bulk crystallization completes the peak height does not change to the maximum temperature. In the $Fe_{78}B_{13}Si_9$ sample at each pressure the rate of increase in peak height with time accelerates through the appearance of the second stage of bulk crystallization. Figure 3 illustrates the calculated temperature for each point in the top graph, with the absolute peak intensity of α-Fe 200 peak and the 202/310 peak for the tetragonal Fe_2B below. Table I lists the summary of observed T_x values for each pressure.

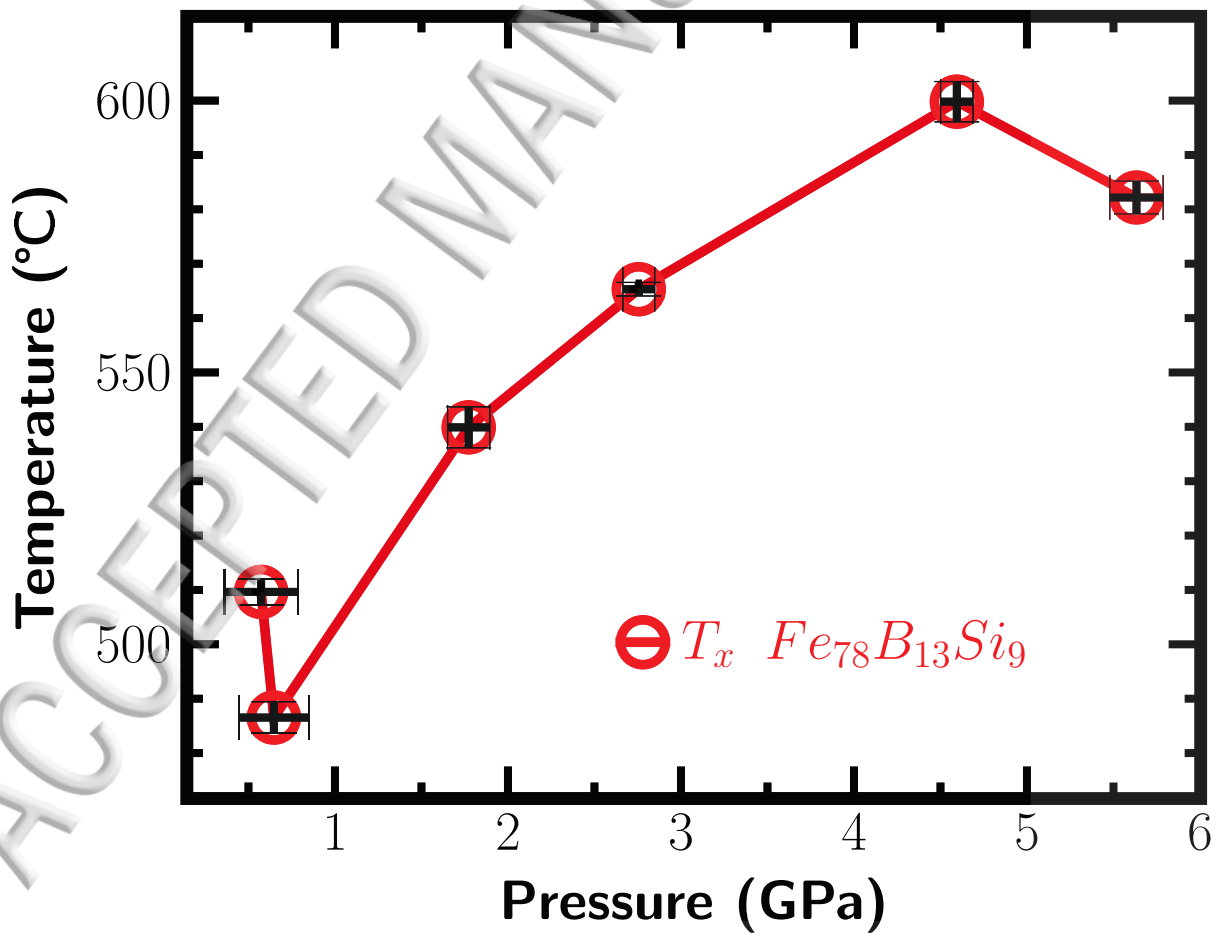

FIG. 4. Crystallization onset T_x for $Fe_{78}B_{13}Si_9$ vs. pressure. The error is shown at each point in black. Values and errors are in table I.

IV. DISCUSSION

The crystal nucleation rate I_ν can be written[16,45]

$$I_\nu = \frac{A_\nu}{\eta(T)} \exp\left(-\frac{\Delta G^*}{k_B T}\right) \tag{1}$$

where η is the viscosity term, A_ν is a constant, k_B is Boltzmann's constant and ΔG^* is the nucleation barrier for forming a spherical nucleus. The nucleation barrier energy ΔG^* can be written[45,46]:

$$\Delta G^* = \frac{\frac{16}{3}\pi\sigma^3}{(P\Delta V + \Delta g)^2} \tag{2}$$

where σ is the inter-facial energy of the nucleus, ΔV change in volume from the liquid to crystalline form, and Δg is the Gibb's free energy difference between the liquid and crystal states. Lower pressures have little effect on the interface energy and $\Delta g \gg P\Delta V$, as a result pressure has minimal effect on the nucleation barrier energy[47,48]. Increase in the onset bulk crystallization temperature can be attributed to the effect of pressure on diffusion activation energy within viscosity term η[45,49]. Figure 4 displays T_x with respect to pressure and indicates a dip in bulk crystallization temperature T_x with a minimum between 0.63 ± 0.20 and 1.77 ± 0.12 GPa.

V. CONCLUSIONS

For each pressure examined bulk crystallization proceeds in two stages in a similar procession to ambient pressure studies. The general increase in onset bulk crystallization temperature $Fe_{78}B_{13}Si_9$ was attributed to increase in diffusion activation energy $Q(T)$ with pressure. An apparent deviation of this trend is found for the first two data points indicating negative pressure dependence of T_x for this range.

VI. ACKNOWLEDGMENTS

We would like to thank Yoshio Kono and the staff of HPcat for all of their help. We would like to acknowledge support from the US National Science Foundation (NSF) under Metals and Metallic Nanostructures program Grant No. DMR-1608682. Portions of this work were performed at HPCAT (Sector 16), Advanced Photon Source (APS), Argonne National Laboratory. HPCAT operations are supported by DOENNSA under award No.

$R_{(°C/min)}$	T_{x1}(℃)	$P_{x1}(GPa)$	T_{x2}(℃)	$P_{x2}(GPa)$	$t_{x2}(s)$	T'_{x1}(℃)	$P'_{x1}(GPa)$	$t'_{x1}(s)$	T'_{x2}(℃)	$P'_{x2}(GPa)$	$t'_{x2}(s)$
2.81	*510 (3)*	*0.57 (21)*	*521 (2)*	*0.58 (22)*	227	*528 (2)*	*0.58 (23)*	377	*527 (2)*	*0.58 (23)*	367
2.74	*487 (3)*	*0.65 (20)*	*496 (3)*	*0.63 (21)*	202	*507 (2)*	*0.61 (23)*	425	*509 (2)*	*0.61 (23)*	451
2.43	*540 (4)*	*1.77 (12)*	*552 (4)*	*1.80 (13)*	257	*561 (2)*	*1.82 (14)*	473	*563 (3)*	*1.82 (14)*	505
2.44	*565 (2)*	*2.76 (09)*	*576 (2)*	*2.79 (10)*	284	*584 (2)*	*2.82 (10)*	472	*584 (2)*	*2.82 (10)*	473
2.26	*600 (4)*	*4.59 (09)*	*610 (2)*	*4.63 (09)*	261	*617 (2)*	*4.65 (10)*	453	*616 (2)*	*4.65 (10)*	430
2.06	*582 (3)*	*5.63 (15)*	*592 (3)*	*5.64 (16)*	224	*598 (2)*	*5.65 (16)*	426	*598 (2)*	*5.65 (16)*	410

TABLE I. For each run, the heating rate (R), (T_{x1}) the onset bulk crystallization temperature for the first stage α-Fe bulk crystallization, (P_{x1}) pressure at the onset bulk crystallization temperature T_{x1}, T_{x2} onset bulk crystallization temperature of the second stage of bulk crystallization, (P_{x2}) pressure at the second stage onset bulk crystallization temperature T_{x2}, (t_{x2}) interval of time from T_{x1} to T_{x2}, (T'_{x1}) the temperature at completion of the first stage α-Fe bulk crystallization, (P'_{x1}) the pressure at completion of the first stage α-Fe bulk crystallization, (t'_{x1}) time from T_{x1} for the completion of α-Fe bulk crystallization, (T'_{x2}) the temperature at completion of the second stage Fe_2B bulk crystallization, (P'_{x2}) the pressure at completion of the second stage Fe_2B bulk crystallization, (t'_{x2}) the time at completion of the second stage Fe_2B bulk crystallization from T_{x1}. The number in parenthesis represents uncertainties in the last digit. Times are rounded to the nearest second. Rate was rounded to the second digit.

DE-NA0001974 with partial instrumentation funding by NSF. The Advanced Photon Source is a U.S. Department of Energy (DOE) Office of Science User Facility operated for the DOE Office of Science by Argonne National Laboratory under Contract No. DE-AC02-06CH11357.

VII. REFERENCES

REFERENCES

[1]W. L. Johnson, "Bulk glass-forming metallic alloys: Science and technology," MRS Bull. **24**, 42–56 (1999).

[2]M. Ashby and A. Greer, "Metallic glasses as structural materials," Scr. Mater. **54**, 321–326 (2006).

[3]D. C. Hofmann, "Bulk metallic glasses and their composites: A brief history of diverging fields," Journal of Materials **2013**, 8 (2013).

[4]S. Madge, "Toughness of bulk metallic glasses," Metals **5**, 1279–1305 (2015).

[5]J. Eckert, J. Das, S. Pauly, and C. Duhamel, "Mechanical properties of bulk metallic glasses and composites," J. Mater. Res. **22**, 285–301 (2007).

[6]A. M. Leary, M. S. Lucas, P. R. Ohodnicki, S. J. Kernion, L. Mauger, C. Park, C. Kenney-Benson, and M. E. McHenry, "The influence of pressure on the phase stability of nanocomposite $Fe_{89}Zr_7B_4$ during heating from energy dispersive x-ray diffraction," J. Appl. Phys. **113**, 17A317 (2013).

[7]H. Y. Tong, B. Z. Ding, H. G. Jiang, S. L. Li, G. S. Li, and J. T. Wang, "Nanostructured transformation mechanism of amorphous Fe-B-Si alloys by the crystallization method," J. Phys. D: Appl. Phys. **27**, 396–401 (1994).

[8]A. R. Yavari and A. Inoue, "Volume effects in bulk metallic glass formation," MRS Proceedings **554** (1998), 10.1557/PROC-554-21.

[9]Y. Li, Q. Guo, J. A. Kalb, and C. V. Thompson, "Matching glass-forming ability with the density of the amorphous phase," Science **322**, 1816–1819 (2008).

[10]D. Miracle, W. Sanders, and O. N. Senkov, "The influence of efficient atomic packing on the constitution of metallic glasses," Philos. Mag. **83**, 2409–2428 (2003).

[11]X. Hu, S. C. Ng, Y. P. Feng, and Y. Li, "Cooling-rate dependence of the density of $Pd_{40}Ni_{10}Cu_{30}P_{20}$ bulk metallic glass," Phys. Rev. B **64**, 172201 (2001).

[12]Q. Hu, X.-R. Zeng, and M. W. Fu, "Characteristic free volumes of bulk metallic glasses: Measurement and their correlation with glass-forming ability," J. Appl. Phys. **109**, 053520 (2011).

[13]M. E. McHenry, M. A. Willard, and D. E. Laughlin, "Amorphous and nanocrystalline materials for applications as soft magnets," Prog. Mater Sci. **44**, 291–433 (1999).

[14]A. H. Taghvaei and J. Eckert, "A comparative study on the isochronal and isothermal crystallization kinetics of $Co_{46.45}Fe_{25.55}Ta_8B_{20}$ soft magnetic metallic glass with high thermal stability," J. Alloys Compd. **675**, 223–230 (2016).

[15]J. Qiao, H. Jia, and P. K. Liaw, "Metallic glass matrix composites," Materials Science and Engineering: R: Reports **100**, 1 – 69 (2016).

[16]J. F. Löffler, "Bulk metallic glasses," Intermetallics **11**, 529 – 540 (2003).

[17]M. Duarte, A. Kostka, D. Crespo, J. Jimenez, A. Dippel, F. Renner, and G. Dehm, "Kinetics and crystallization path of a fe-based metallic glass alloy," Acta Mater. **127**,

341–350 (2017).

[18]P. Ramasamy, A. Szabo, S. Borzel, J. Eckert, M. Stoica, and A. Bárdos, "High pressure die casting of fe-based metallic glass," Sci. Rep. **6**, 35258 (2016).

[19]L. Liu, J. Ma, C. Yu, X. Huang, L. He, L. Zhang, P. Li, and Z. Liu, "Determination of forming ability of high pressure die casting for zr-based metallic glass," J. Mater. Process. Technol. **244**, 87 – 96 (2017).

[20]E. Illekova, I. Mat'Ko, P. Duhaj, and F.-A. Kuhnast, "The complex characteristics of crystallization of the $Fe_{75}Si_{15}B_{10}$ glassy ribbon," J. Mater. Sci. **32**, 4645–4654 (1997).

[21]C. Yang, W. K. Wang, R. P. Liu, Z. J. Zhan, L. L. Sun, J. Zhang, J. Z. Jiang, L. Yang, and C. Lathe, "Crystallization of $Zr_{41}Ti_{14}Cu_{12.5}Ni_{10}Be_{22.5}$ bulk metallic glass under high pressure examined by *in situ* synchrotron radiation x-ray diffraction," J. Appl. Phys. **99**, 023525 (2006).

[22]Y. X. Zhuang, J. Z. Jiang, T. J. Zhou, H. Rasmussen, L. Gerward, M. Mezouar, W. Crichton, and A. Inoue, "Pressure effects on $Al_{89}La_6Ni_5$ amorphous alloy crystallization," Appl. Phys. Lett. **77**, 4133–4135 (2000).

[23]J. Y. Bang and R. Y. Lee, "Crystallization of the metallic glass $fe_{78}b_{13}si_9$," J. Mater. Sci. **26**, 4961–4965 (1991).

[24]G. Shen, P. Chow, Y. Xiao, S. Sinogeikin, Y. Meng, W. Yang, H.-P. Liermann, O. Shebanova, E. Rod, A. Bommannavar, and H.-K. Mao, "Hpcat: An integrated high-pressure synchrotron facility at the advanced photon source," High Pressure Res. **28**, 145–162 (2008).

[25]A. P. Hammersley, S. O. Svensson, M. Hanfland, A. N. Fitch, and D. Hausermann, "Two-dimensional detector software: From real detector to idealised image or two-theta scan," High Pressure Res. **14**, 235–248 (1996).

[26]F. Birch, "Finite strain isotherm and velocities for single-crystal and polycrystalline NaCl at high pressures and 300 K," Journal of Geophysical Research: Solid Earth **83**, 1257–1268 (1978).

[27]N. Velisavljevic and Y. K. Vohra, "Distortion of α-uranium structure in praseodymium metal to 311 GPa," High Pressure Res. **24**, 295–302 (2004).

[28]Y. Kono, C. Park, C. Kenney-Benson, G. Shen, and Y. Wang, "Toward comprehensive studies of liquids at high pressures and high temperatures: Combined structure, elastic wave velocity, and viscosity measurements in the paris-edinburgh cell," Phys. Earth Planet. Inter. **228**, 269 – 280 (2014).

[29]A. Yamada, Y. Wang, T. Inoue, W. Yang, C. Park, T. Yu, and G. Shen, "High-pressure x-ray diffraction studies on the structure of liquid silicate using a paris-edinburgh type large volume press," Rev. Sci. Instrum. **82**, 015103 (2011).

[30]A. K. Stemshorn, *Devitrification of Iron Based Metallic Glasses at High Pressures and High Temperatures*, Ph.D. thesis (2014).

[31]Y. Kono, T. Irifune, Y. Higo, T. Inoue, and A. Barnhoorn, "P–v–t relation of MgO derived by simultaneous elastic wave velocity and *in situ* x-ray measurements: A new pressure scale for the mantle transition region," Phys. Earth Planet. Inter. **183**, 196–211 (2010).

[32]P. I. Dorogokupets, "P–V–T equations of state of MgO and thermodynamics," Phys. Chem. Miner. **37**, 677–684 (2010).

[33]Y. Ye, V. Prakapenka, Y. Meng, and S.-H. Shim, "Intercomparison of the gold, platinum, and MgO pressure scales up to 140 GPa and 2500 K," Journal of Geophysical Research: Solid Earth **122**, 3450–3464 (2017).

[34]P. Ballirano and R. Caminiti, "Rietveld refinements on laboratory energy dispersive x-ray diffraction (EDXD) data," J. Appl. Crystallogr. **34**, 757–762 (2001).

[35]B. H. Toby, "*CMPR* – a powder diffraction toolkit," J. Appl. Crystallogr. **38**, 1040–1041 (2005).

[36]W. Kraus and G. Nolze, "*POWDER CELL* – a program for the representation and manipulation of crystal structures and calculation of the resulting x-ray powder patterns," J. Appl. Crystallogr. **29**, 301–303 (1996).

[37]M. Ohnuma, O. Sasaki, H. Kuwano, S. Katano, Y. Morii, S. Funahashi, H. R. Child, and Y. Hamaguchi, "Crystallization process of $(Fe_{80}P_{20})_xSi_y$ amorphous alloys," Mater. Trans., JIM **34**, 874–881 (1993).

[38]R. V. Ramanujan and Y. R. Zhang, "Solid state dendrite formation in an amorphous magnetic $Fe_{77.5}Si_{13.5}B_9$ alloy observed by *in situ* hot stage transmission electron microscopy," Appl. Phys. Lett. **88**, 182506 (2006).

[39]W. K. Wang, H. Iwasaki, and K. Fukamichi, "Effect of high pressure on the crystallization of an amorphous $Fe_{83}B_{17}$ alloy," J. Mater. Sci. **15**, 2701–2708 (1980).

[40]S. Guo and C. Su, "Micro-nano ductile-phases reinforced fe-based bulk metallic glass matrix composite with large plasticity," Materials Science and Engineering: A **707**, 44–50 (2017).

[41]D. M. Minić, V. A. Blagojević, D. M. Minić, and T. Žák, "Influence of microstructural inhomogeneity of individual sides of $Fe_{81}Si_4B_{13}C_2$ amorphous alloy ribbon on thermally induced structural transformations," Mater. Chem. Phys. **130**, 980–985 (2011).

[42]R. C. O'Handley, "Physics of ferromagnetic amorphous alloys," J. Appl. Phys. **62**, R15–R49 (1987).

[43]K. Lu, "Nanocrystalline metals crystallized from amorphous solids: Nanocrystallization, structure, and properties," Materials Science and Engineering: R: Reports **16**, 161–221 (1996).

[44]F. M. Wang and R. Ingalls, "Iron bcc-hcp transition: Local structure from x-ray-absorption fine structure," Phys. Rev. B **57**, 5647–5654 (1998).

[45]W. H. Wang, Z. X. Wang, D. Q. Zhao, M. B. Tang, W. Utsumi, and X.-L. Wang, "High-pressure suppression of crystallization in the metallic supercooled liquid $Zr_{41}Ti_{14}Cu_{12.5}Ni_{10}Be_{22.5}$: Influence of viscosity," Phys. Rev. B **70**, 092203 (2004).

[46]J. Z. Jiang, L. Gerward, and Y. S. Xu, "Pressure effect on crystallization kinetics in $Zr_{46.8}Ti_{8.2}Cu_{7.5}Ni_{10}Be_{27.5}$ bulk metallic glass," Appl. Phys. Lett. **81**, 4347–4349 (2002).

[47]Z. Han, X. Huang, A. A. Luo, A. K. Sachdev, and B. Liu, "A quantitative model for describing crystal nucleation in pressurized solidification during squeeze casting," Scr. Mater. **66**, 215–218 (2012).

[48]A. Setyawan, H. Kato, J. Saida, and A. Inoue, "Evidence for effect of hydrostatic pressure during casting on glass-forming ability in $(Zr_{65}Al_{7.5}Ni_{10}Cu_{17.5})_{1-x}Pd_x$ (x=0-17.5) alloys," Materials Science and Engineering: A **449**, 903 – 906 (2007).

[49]R. S. J., "New challenges for the pressure evolution of the glass temperature," Front. Mater. **4**, 33 (2017).

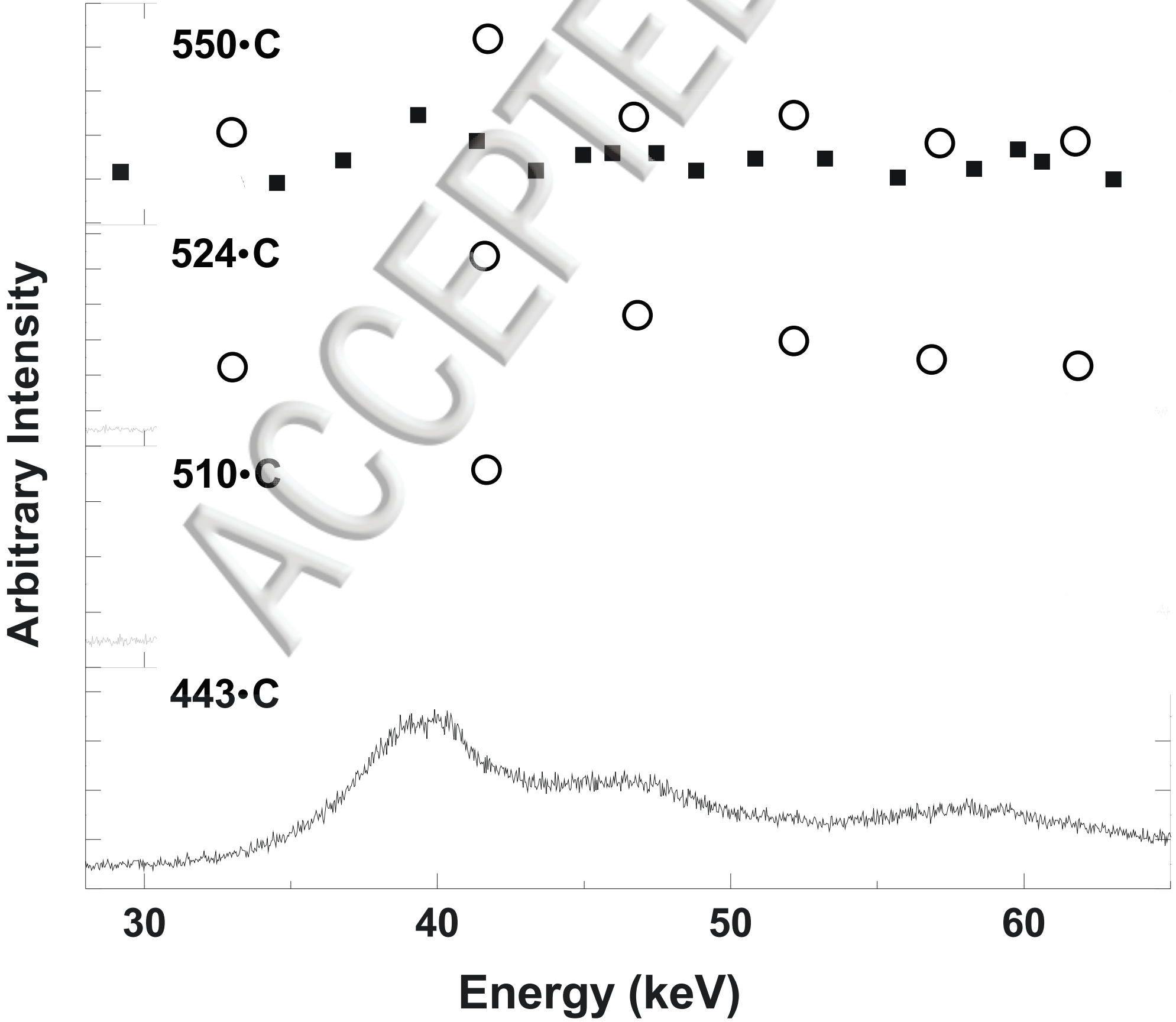
550•C
524•C
510•C
443•C
Arbitrary Intensity
30
40
50
60
Energy (keV)

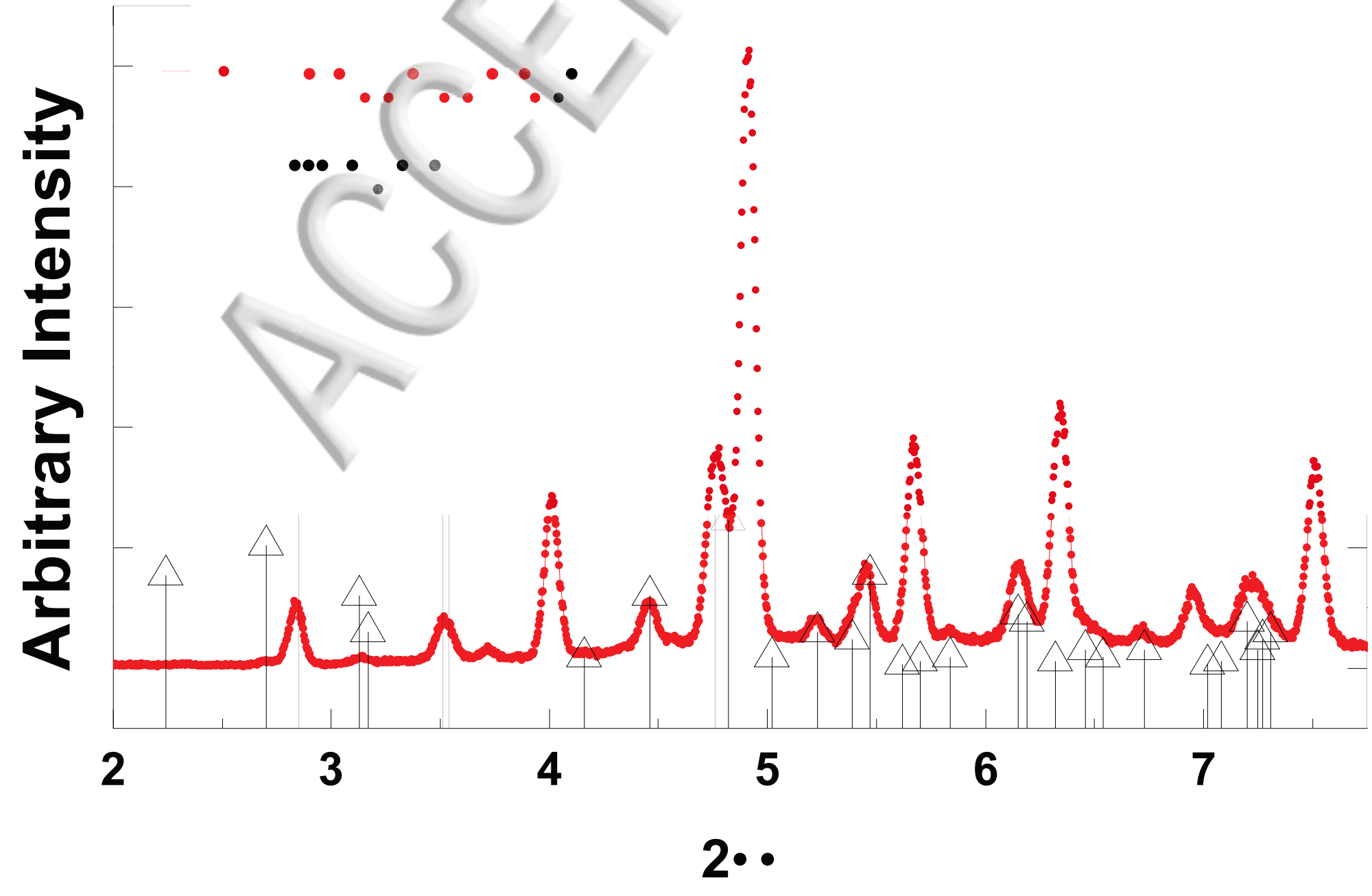
Arbitrary Intensity
2
3
4
5
6
7
2• •

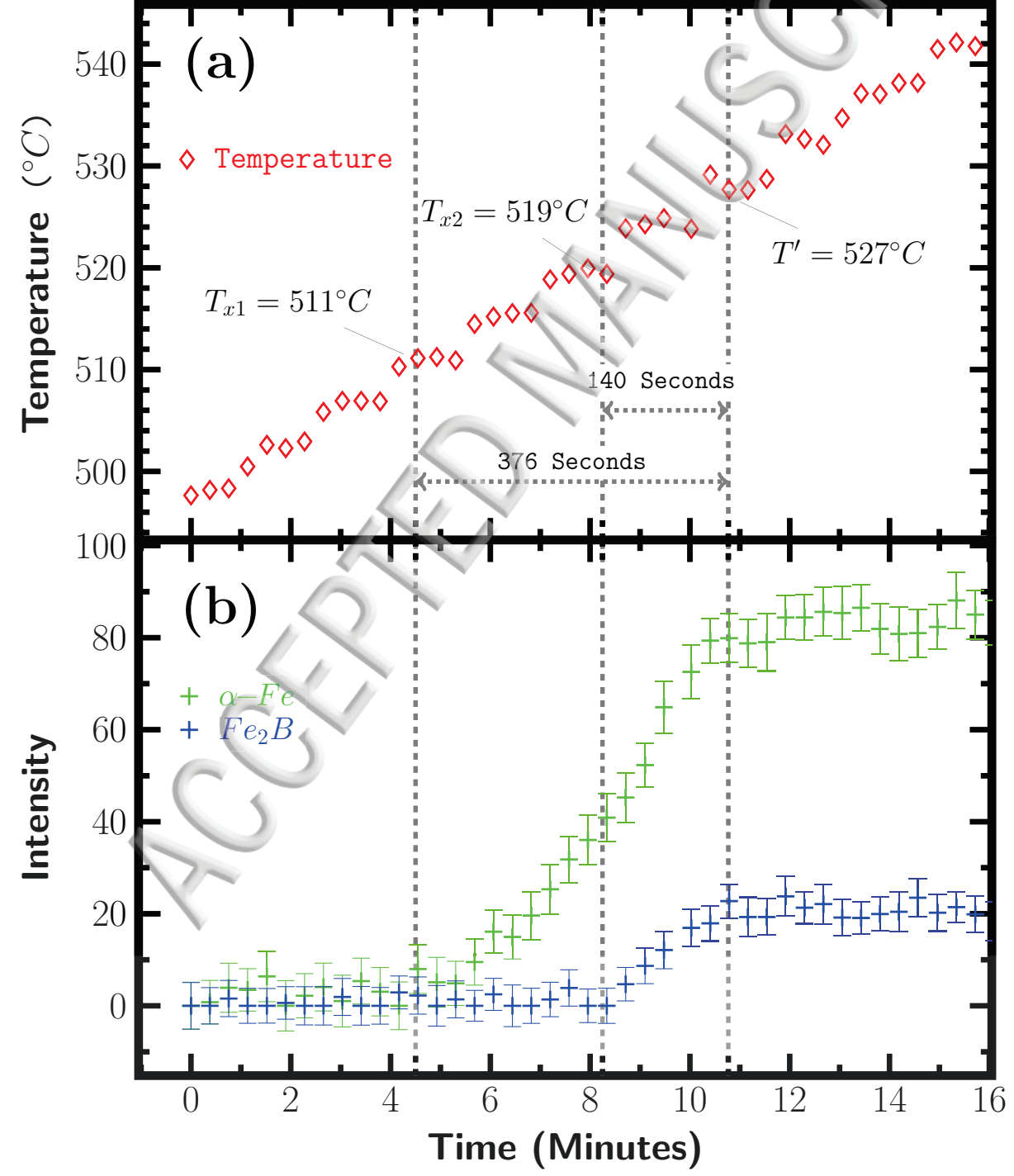

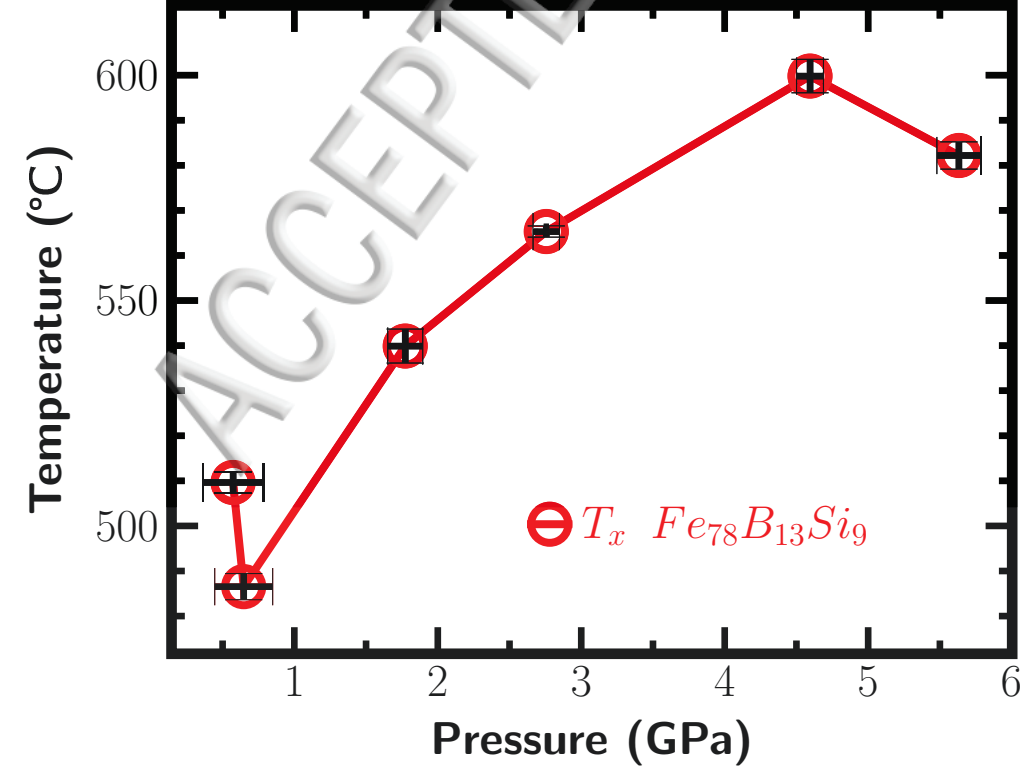
Temperature (°C)
600
550
500
1
2
3
4
5
6
Pressure (GPa)
T_x $Fe_{78}B_{13}Si_9$